Icarus 382 (2022) 115021

Contents lists available at ScienceDirect

Icarus

journal homepage: www.elsevier.com/locate/icarus

Research Paper

Spectral evidence for a pyroclastic mantle over the Tacquet formation and Menelaus domes of southwest Mare Serenitatis

William H. Farrand [a,*], Christopher S. Edwards [b], Christian Tai Udovicic [b]

[a] Space Science Institute, 4765 Walnut Street, Suite B, Boulder, CO 80301, USA
[b] Department of Astronomy and Planetary Science, Northern Arizona University, Flagstaff, AZ 86011, USA

ARTICLE INFO

Keywords:
Lunar pyroclastic deposits
Reflectance spectroscopy
Lunar volcanism

ABSTRACT

The Tacquet Formation (TF) was first identified in geologic mapping of southern Mare Serenitatis as a distinct low albedo region split by the linear Rimae Menelaus rilles. A distinct western dome, split by a linear rille and less distinct eastern dome (the Menelaus domes) are also present within the TF. Previous Earth-based radar analyses showed that the TF has a lower circular polarization ratio consistent with a pyroclastic mantle. In this study, compositional and spectroscopic parameters were derived from Moon Mineralogy Mapper (M^3) data. Lunar Reconnaissance Orbiter Camera Wide Angle Camera (LROC WAC) and SELENE Kaguya Multiband Imager (MI) multispectral data were also utilized. FeO derived from MI data for the TF and Menelaus domes was elevated at levels consistent with pyroclastic glasses. While not diagnostic of pyroclastics, TiO_2 derived from LROC WAC data over the TF and Menelaus domes was also elevated relative to the background materials. Analysis of 1 and 2 μm band parameters also show the TF and Menelaus domes as being distinct with a band center moderately longer than 1 μm and 2 μm band center shorter than the surroundings, characteristics consistent with pyroclastic glass and/or increased ilmenite. M^3 data thermally corrected via two different thermal correction approaches indicate a moderately deeper band in the 3 μm region indicative of OH and/or H_2O, a characteristic that is also potentially associated with pyroclastic deposits. These compositional findings are consistent with the Earth-based radar data suggesting that the TF is a pyroclastic mantle and potentially represents a previously unrecognized sub-class of pyroclastic deposits associated with lunar volcanic domes.

1. Introduction and geologic background

Lunar volcanism has produced distinct landforms and features including the flood basalts making up the lunar maria, volcanic vents, mantling lunar pyroclastic deposits, and constructional features such as lunar domes. While some of these features have been linked, such as vents for the eruption of pyroclastic deposits, or domes occurring on maria, two that have generally not been associated are lunar pyroclastic deposits (LPDs) and domes. In this paper, the association of domes, the Menelaus domes of southern Mare Serenitatis (Fig. 1); Lena et al. (2013) and the dark-toned Tacquet Formation, hypothesized by Carter et al. (2009) as a form of pyroclastic mantle, are examined. In this instance, the type of pyroclastic deposit that is in question is a localized deposit (e.g., Hawke et al., 1989; Gaddis et al., 2003; Trang et al., 2017) defined as a deposit <2500 km^2 in areal extent. Localized LPDs are generally associated with floor-fractured craters, but have been found in other geologic settings as well. Gustafson et al. (2012) used Lunar Reconnaissance Orbiter Camera Narrow Angle Camera (LROC NAC) imagery to detect a number of previously unrecognized LPDs including one associated with the Rima Birt linear rille. This deposit has also been examined by Besse et al. (2014) and Trang et al. (2017, 2021). Like the Menelaus domes in the Tacquet Formation, there are two domes split by linear rilles associated with the Birt E rille segment. These were noted by both Lena et al. (2013) and by Trang et al. (2017). The latter set of authors considered the Rima Birt domes to be constructional features of the pyroclastic eruption. The LPD associated with the Tacquet formation is potentially in a class with the Rima Birt deposit in that it is associated with the linear "Rimae Menelaus" rilles as well as covering the Menelaus domes although whether the Menelaus domes are constructs of erupted pyroclastic material or domes built by effusive eruptions that were mantled by a later pyroclastic stage of activity is not determinable from the available data.

The Tacquet Formation was first described in the Carr (1966) geologic map of the Mare Serenitatis region (Fig. 1B). Carr (1966)

* Corresponding author.
E-mail address: farrand@spacescience.org (W.H. Farrand).

https://doi.org/10.1016/j.icarus.2022.115021
Received 25 February 2022; Received in revised form 23 March 2022; Accepted 31 March 2022
Available online 8 April 2022

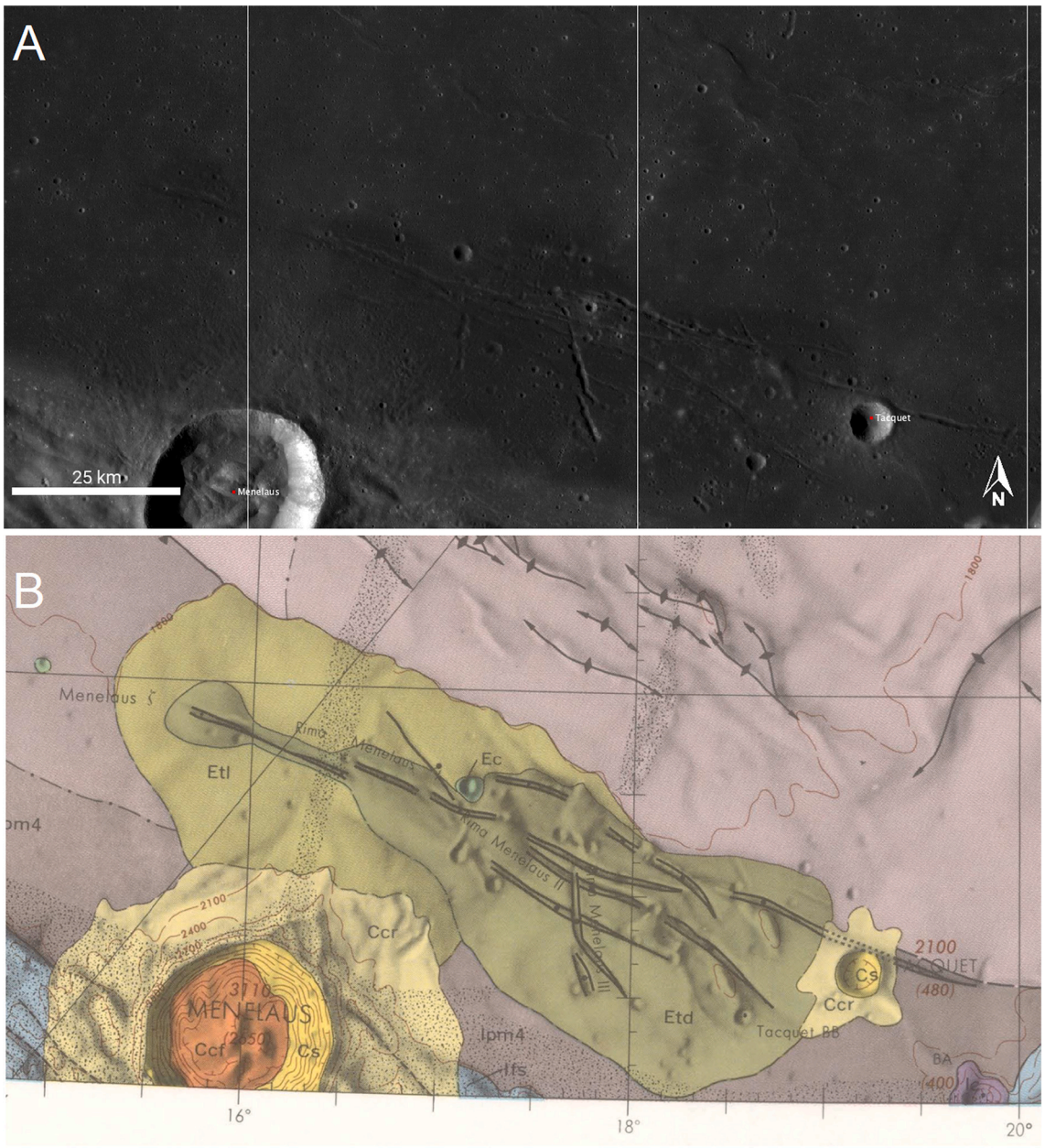

Fig. 1. A. View of southern Mare Serenitatis with WAC mosaic basemap (from JMARS). B. Portion of Carr (1966) geologic map of Mare Serenitatis over approximately the same area as in A. The Tacquet Formation dark member (Etd) is in dark green and its light member (Etl) is in light green. (For interpretation of the references to color in this figure legend, the reader is referred to the web version of this article.)

categorized it as being Eratosthenian in age and divided it into a dark (Etd) and light (Etl) member, and he interpreted it as being composed of "volcanic flows and pyroclastics derived in part from the Menelaus rilles". The Menelaus rilles (or "Rimae Menelaus") are a set of linear rilles that criss-cross the area under consideration here. The Tacquet Formation itself extends over an area from approximately 16.1 to 18.1° N and 15 to 19° E (to the namesake 6.3 km crater, Tacquet). The Menelaus rilles extend to the east beyond the area described by Carr (1966) out to approximately 21° E. In the unified geologic map of the Moon of Fortezzo et al. (2020), the TF is not included as a separate unit, but falls within their broader Eratosthenian mare (Em) unit that covers the arcuate southern portion of Mare Serenitatis. The Em unit is likewise described as consisting of "relatively thin, young volcanic flows or pyroclastic material". Carter et al. (2009) used 12.6 cm wavelength S band radar data transmitted from Arecibo to find that the TF has a low circular polarization ratio of 0.18 ± 0.06 which they described as comparable to the known Sulpicius Gallus LPD. Occurring within the confines of the TF are the Menelaus domes- (named with reference to the 27 km diameter Menelaus crater to the south) described by Lena et al. (2013). Those authors referenced "Menelaus 1" and "Menelaus 2" domes which correspond to a dome centered near 17.8°N, 15.65°E and one centered near 17.5°N, 16.6°E. Examination of the LOLA/Kaguya merged topography (Barker et al., 2016) indicates that the Menelaus 1 dome to the west is truly a dome. However, the LOLA/Kaguya merged topography indicates that the area including the Menelaus 2 "dome" is the northwestern corner of a general rise in elevation bisected by linear rilles and what Lena et al. (2013) called the Menelaus 2 "dome" is an ovoidal low albedo region bordered on the south by a rille that gives it the appearance of a dome. While its characterization as a "dome" is problematic, the region including it is still described in this paper as the eastern Menelaus "dome". In their survey of lunar domes, Lena et al. (2013) grouped the Menelaus domes in their category of "effusive domes

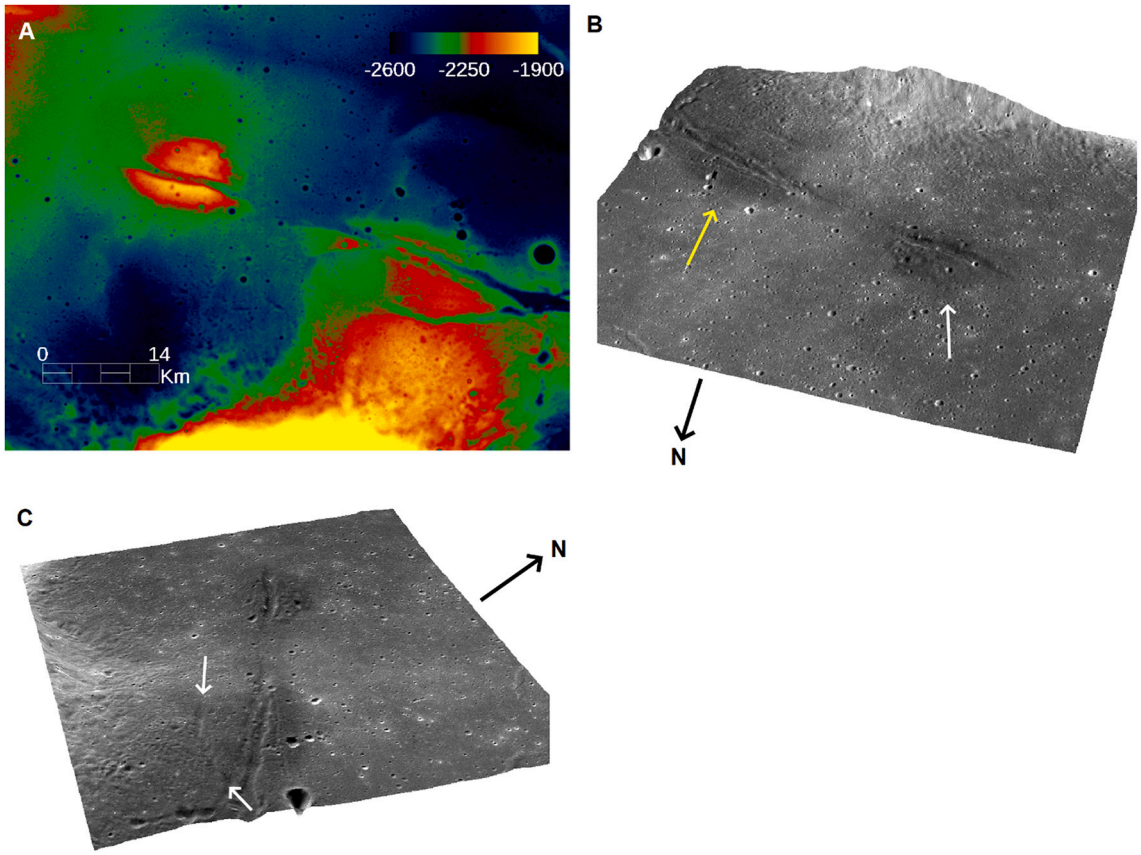

Fig. 2. A. Pseudo-colored LOLA/Kaguya TC DEM over the Tacquet Formation and Menelaus domes. B. Perspective view of 100 m/pixel WAC global mosaic overlain on LOLA/Kaguya TC DEM (from A) with 12× vertical exaggeration looking south (black arrow indicating north outside of image) with Menelaus dome 1 indicated by white arrow and the purported Menelaus dome 2 of Lena et al. (2013) indicated by yellow arrow. C. Perspective view looking west (black arrow indicating north outside of image). The rille on the south border of the eastern "dome", that gives it the appearance of being a dome rather than part of a general platform, is indicated by opposing white arrows. (For interpretation of the references to color in this figure legend, the reader is referred to the web version of this article.)

bisected by linear rilles". The western Menelaus 1 dome is split by a linear rille as is the eastern Menelaus 2 "dome" (Fig. 2).

Carr (1966) noted that the dark TF member has a very low albedo (0.05–0.06); however, results from orbital spacecraft of the last two decades have revealed other compositionally distinctive characteristics of Carr's Etd unit. Besides having a lower albedo than the surroundings (Fig. 3A), these include: elevated FeO abundance values in the Kaguya MI mapping of global FeO (Fig. 3B), low values in the Kaguya MI mapping of global clinopyroxene abundance (Fig. 3C) (Lemelin et al., 2016), and elevated TiO_2 (Fig. 3D) as derived from LROC WAC data (Sato et al., 2017). The FeO analysis is carried out below using the VNIR channels at 20 m/pixel resolution versus the 60 m/pixel resolution of the Lemelin et al. (2016) maps. Likewise, TiO_2 is elevated over the broader Eratosthenian mare (Em) unit of Fortezzo et al. (2020) in the Sato et al. (2017) TiO_2 map at 400 m/pixel, but in the higher spatial resolution WAC data presented below, at the VNIR resolution of 75 m/pixel, the Etd unit, that is coincident with the white dash-dot outlined area in Fig. 3, has higher TiO_2 than the surrounding Em unit.

In this paper, we assess the Tacquet Formation area that includes the Menelaus dome(s) and the rille fractured area to the east and their context within the broad Em map unit of Fortezzo et al. (2020). Low spatial resolution global measures of several compositional parameters are presented in Fig. 3, but we have generated higher spatial resolution mappings of these parameters and other compositional characteristics using Moon Mineralogy Mapper (M^3), SELENE Kaguya Multiband Imager (MI), and Lunar Reconnaissance Orbiter Camera Wide Angle Camera (LROC WAC) multispectral data. We use these data to describe the composition of the materials considered and their geologic history.

2. Datasets

2.1. Kaguya Multiband Imager

Kaguya MI is a multispectral instrument consisting of two cameras, a UV–Vis camera with bands largely duplicative of the Clementine instrument (McEwen and Robinson, 1997) centered at 415, 750, 900, 950, and 1001 nm, and a NIR camera with bands centered at 1000, 1050, 1250, and 1550 nm. The spatial resolution of the UV–Vis camera is 20 m/pixel and that of the NIR camera is 62 m/pixel. The MI data used in this study is from the MAP processing level in which the data have been mosaiced and georeferenced to tiles in a simple cylindrical projection. The data is in scaled reflectance. The processing of the MI MAP data is described by Ohtake et al. (2013).

As alluded to above, the MI data has been used by Lemelin et al. (2015 and 2019) for the derivation of weight percent FeO in a fashion adapted from that used for Clementine data by Lucey et al. (2000) and that methodology is used here as well. With regards to trying to assess if the putative mantle constituting the Tacquet Formation is pyroclastic in origin, FeO is an important parameter. Glass can be a major constituent of pyroclastic ash, and, as noted by Allen et al. (2012), FeO is elevated in lunar glasses. That study cites the work of Delano (1986) who observed that glasses returned by Apollo astronauts ranged from 16.5 to 24.7 wt% FeO. This is contrasted with Lunar Prospector Gamma Ray Spectrometer (LP-GRS) data that for southern Mare Serenitatis the mare has approximately 12 to 15 wt% FeO (Lawrence et al., 2002). Thus, evidence of FeO abundances greater than surrounding mare basalts is potentially indicative of a significant glass component. We note however that if the TF

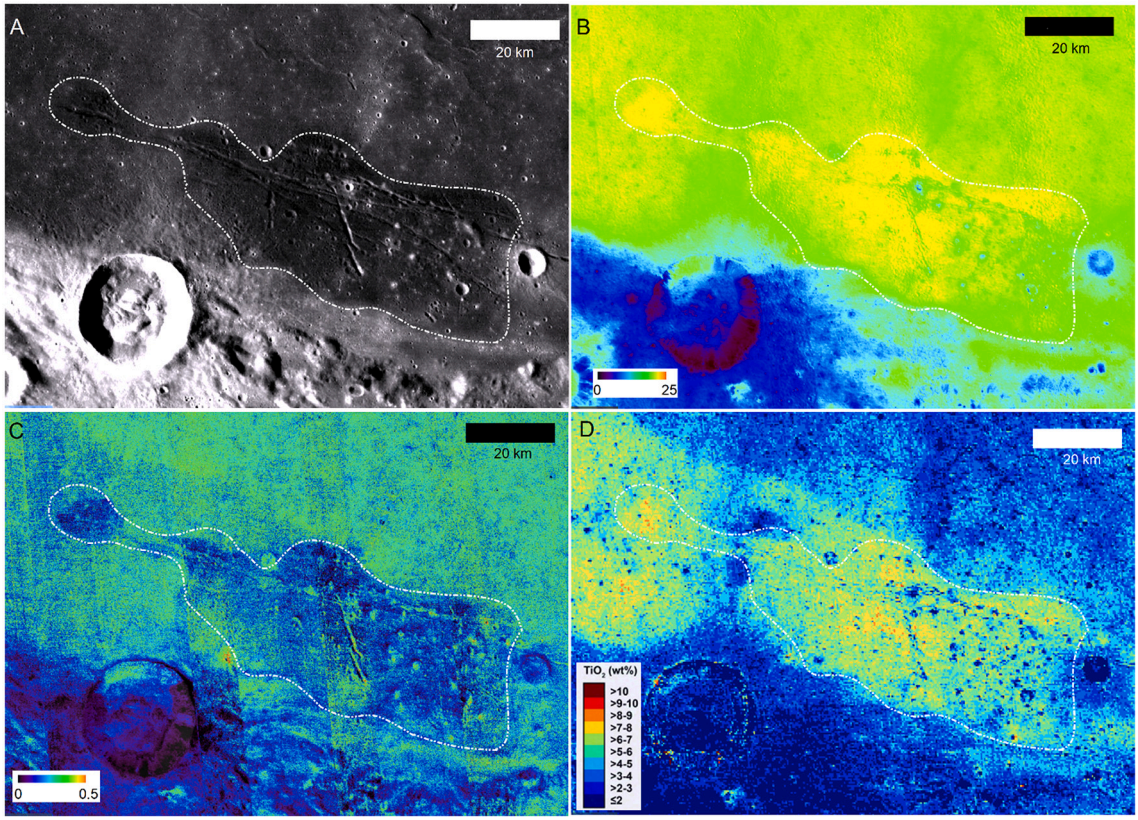

Fig. 3. Distinctive albedo and compositional properties of the Menelaus domes area and of the encompassing Tacquet Formation from global maps in ASU Quickmap web interface. Area with spectral properties different from surroundings is outlined in white. A. LROC WAC global mosaic view. B. Weight percent FeO from Kaguya MI. C. Clinopyroxene abundance from Kaguya MI. D. Weight percent TiO_2 from LROC WAC.

does indeed have a major pyroclastic component that the algorithm for derivation of FeO from optical data is not quantitative for pyroclastic deposits. This is based on the chemical similarity of orange glass and black bead (rapidly cooled versus more slowly cooled materials) deposits, but their highly different optical character (Wilcox et al., 2006). Nevertheless, while the weight percent FeO values derived from the optical data over pyroclastics is not strictly quantitative, it does provide a qualitative measure of compositional distinctiveness from surrounding materials.

2.2. LROC Wide Angle Camera

The Lunar Reconnaissance Orbiter Camera (LROC) consists of a monochromatic Narrow Angle Camera (NAC) with high (50 cm/pixel from a 50 km orbit) spatial resolution and a multispectral Wide-Angle Camera (WAC). The WAC has two UV bands centered at 321 and 360 nm with a spatial resolution of 384 m/pixel from a 50 km altitude and five Vis bands centered at 415, 566, 604, 643, and 689 nm with a spatial resolution of 75 m/pixel from a 50 km altitude (Robinson et al., 2010). The WAC data is useful for the derivation of weight percent TiO_2 (Sato et al., 2017; Hapke et al., 2019), the mapping of a primary TiO_2 host mineral, ilmenite, and as a complement to other orbital multi- and hyperspectral datasets for the mapping of primary silicate minerals.

2.3. Moon Mineralogy Mapper (M^3)

The M^3 instrument, that was on-board the Indian Chandrayaan-1 spacecraft (e.g., Pieters et al., 2009), was an imaging spectrometer capable of operating in both a global and a targeted mode. The global mode consisted of 85 spectral channels from 460 to 2790 nm with low signal-to-noise ratio in the first two bands (making it effectively an 83-channel dataset from 540 to 2790 nm). The targeted mode had higher spatial and spectral resolution, but targeted scenes were not collected over the southern Mare Serenitatis area and so are not relevant here. M^3 data was collected over several distinct orbital periods dictated by the operations of the Chandrayaan-1 spacecraft. Here we work with two adjoining scenes: M3G20090108T04465 and M3G20090204T094731 and one that includes terrain covered in both of those scenes, M3G20090204T113444. M3G20090108T04465 was collected during "Optical Period" (OP) 1, M3G20090204T094731 and M3G20090204T113444 during OP-1b. All were collected from a 100 km orbital altitude yielding a spatial resolution of 140 m/pixel and since all were collected from relatively early in the M^3 data collection mission, all are of similar quality with respect to qualitatively assessed signal-to-noise ratio.

The M^3 data were analyzed using several approaches. Fig. 3C shows a mapping of clinopyroxene abundance generated by (Lemelin et al., 2016) from Kaguya MI data. Using full spectral resolution M^3 data allows for a more detailed mapping of the crystal field bands centered near 1 and 2 μm which could be caused by pyroxene, or, especially in the case of possible pyroclastics, by the presence of glass. Moriarty and Pieters (2016) described a parabola and linear continuum (PLC) technique to approximate the 1 and 2 μm band minima and their associated band depths. A related approach, the "Wavelength Mapper" (WM), originally developed for use with Mars Express OMEGA data (van Ruitenbeek et al., 2014) and later used with terrestrial airborne hyperspectral remote sensing data (Hecker et al., 2019) was used in this study. The implementation of WM used is incorporated in the HypPy (Hyperspectral Python) package (Bakker et al., 2014). In the WM, first, a convex hull is fit over the specified wavelength range; for the 1 μm region this was 0.75 to 1.21 μm, and for the 2 μm region, this was 1.55 to 2.7 μm and is divided out. Similarly to Moriarty and Pieters (2016), a

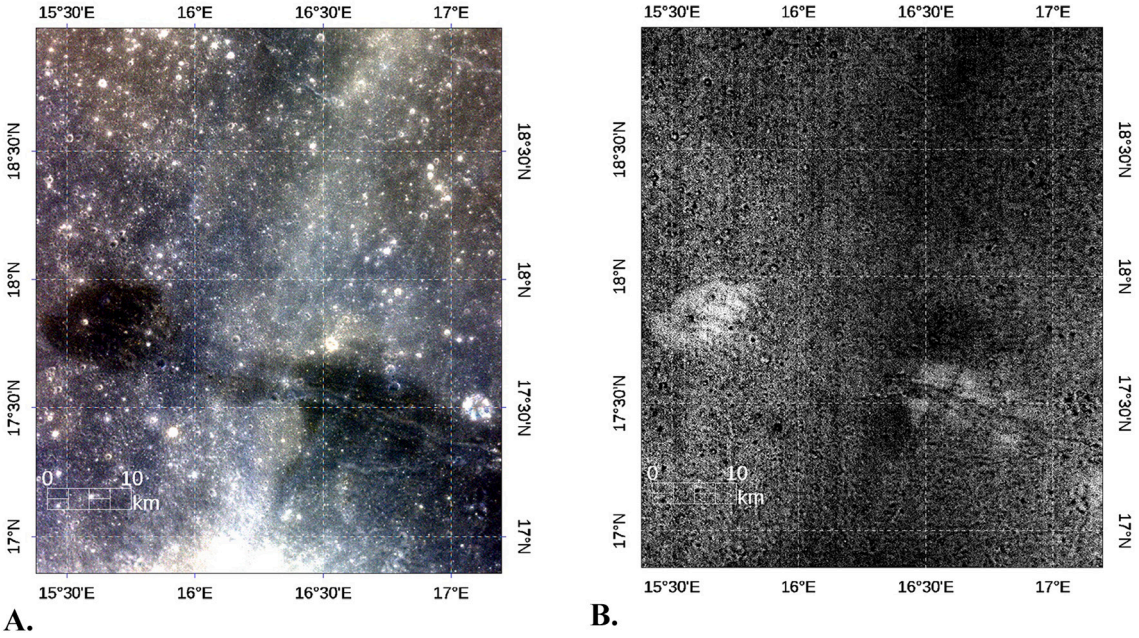

Fig. 4. A. Composite of 689, 566, and 415 nm bands for a subsection of LROC WAC scene M139802168 centered on the Menelaus domes. B. the 321 nm/415 nm ratio image for the same subsection showing elevated data numbers, indicative of higher TiO_2, over the domes.

second order polynomial is then fit to three consecutive bands with the center band having the lowest reflectance in the spectral range covering the absorption feature. The minimum wavelength position is the interpolated minimum of the parabola fit to those three bands. Also, a band depth (the continuum value of 1.0 minus the continuum-removed band minimum reflectance) is derived.

At wavelengths longer than 2 μm under midday sun, thermal emission contributes to the radiance leaving the lunar surface. There is no universally agreed upon approach to thermal correction of M^3 data at these longer wavelengths. Initial efforts at a thermal correction approach were those of Clark et al. (2011). The Clark et al. (2011) correction relies on a linear extrapolation from shorter wavelength portions of the reflectance spectrum (not affected by thermal emission) and derives a surface temperature (the thermal emission component) from the difference between the measured and extrapolated spectrum. The Clark et al. (2011) correction also assumes an isothermal surface. Clark et al. (2011) also noted potential issues for the correction in pyroxene-rich terrains and additional shortcomings of the approach were discussed by McCord et al. (2011) who noted that it underestimated surface temperatures. Other studies have also found that temperatures derived from the Clark et al. (2011) correction underestimate surface temperatures by ~10 to 30 K (Li and Milliken, 2016; Bandfield et al., 2018; Tai Udovicic et al., 2020). The empirical approach to thermal correction by Li and Milliken (2016) uses reflectance spectra from the Apollo sample soil collection to define a relationship between the reflectance at 1.55 μm and that at 2.54 μm. They use this relation to predict thermal excess in M^3 spectra at 2.54 μm and, when present, correct for it. Photometric and topographic corrections are also applied to the data in their approach, but they assume an isothermal surface. Bandfield et al. (2018) and Wöhler et al. (2017) have accounted for the anisothermal nature of the lunar surface by incorporating roughness models which account for the cm-scale, unresolved surface roughness. Due to the low thermal inertia and lack of atmosphere, surfaces directly adjacent to one another may have dramatically different temperatures (e.g., 100 s of K). These temperatures are then integrated for a distribution of slope and azimuths for a range of roughnesses (typically ~20° RMS slope, Bandfield et al., 2015, 2018) to predict the "rough radiance" around the 3 μm region which is then removed to produce a reflectance spectrum (Bandfield et al., 2018). Given uncertainties about the thermal correction of M^3 data, data corrected via both the Li and Milliken (2016) and the Bandfield et al. (2018) (as updated by Tai Udovicic et al., 2021) approaches are considered here.

Milliken and Li (2017) described apparent hydration (in the form of a steeper dropoff of reflectance longwards of 2.65 μm) of several lunar pyroclastic deposits based on their custom Li and Milliken (2016) thermal correction approach. In the analysis of Bandfield et al. (2018) a dropoff in reflectance near 3 μm was more evenly distributed across the lunar surface, including between both the LPDs and the surroundings with increased hydration of the three LPDs examined, Aristarchus Plateau, Sinus Aestuum, and Sulpicius Gallus, being more subtle. In this study, the M^3 M3G20090204T094731 scene was thermally corrected using the methodology of Bandfield et al. (2018) and recently refined by Tai Udovicic et al. (2019, 2020, 2021). For comparison, that scene was also corrected via the approach of Li and Milliken (2016) with the thermally corrected data provided courtesy of Dr. S. Li.

Another approach that also takes into account the anisothermal nature of the lunar surface is that of Wöhler et al. (2017). In that study, to assess the level of possible hydration (presence of OH and/or H_2O) Wöhler et al. (2017) used a metric of the integrated depth of dropoff of reflectance from a straight-line continuum from 2.65 to 2.97 μm as a measure of the relative abundance of OH, and possibly H_2O (an OH integrated band depth, OHIBD). A simple band ratio of 2736 nm / 2816 nm has also been used as an assessment of the level of potential hydration (Petro et al., 2013). However, in this study, the OHIBD was applied to the thermally corrected M3G20090204T094731 scene examined here and OHIBD values are used as a gauge of the approximate level of hydration. Milliken and Li (2017) and Li and Milliken (2017) use the effective single-particle absorption thickness (ESPAT) parameter of Hapke (2012) to gauge the level of hydration; however, as noted by Klima and Petro (2017) multiple uncertainties are inherent in modeling the ESPAT parameter. Thus, the use of the relative measure of OHIBD is deemed more straightforward in this instance.

3. Results

3.1. LROC WAC

The global WAC TiO_2 map (at a spatial resolution of 399 m/pixel),

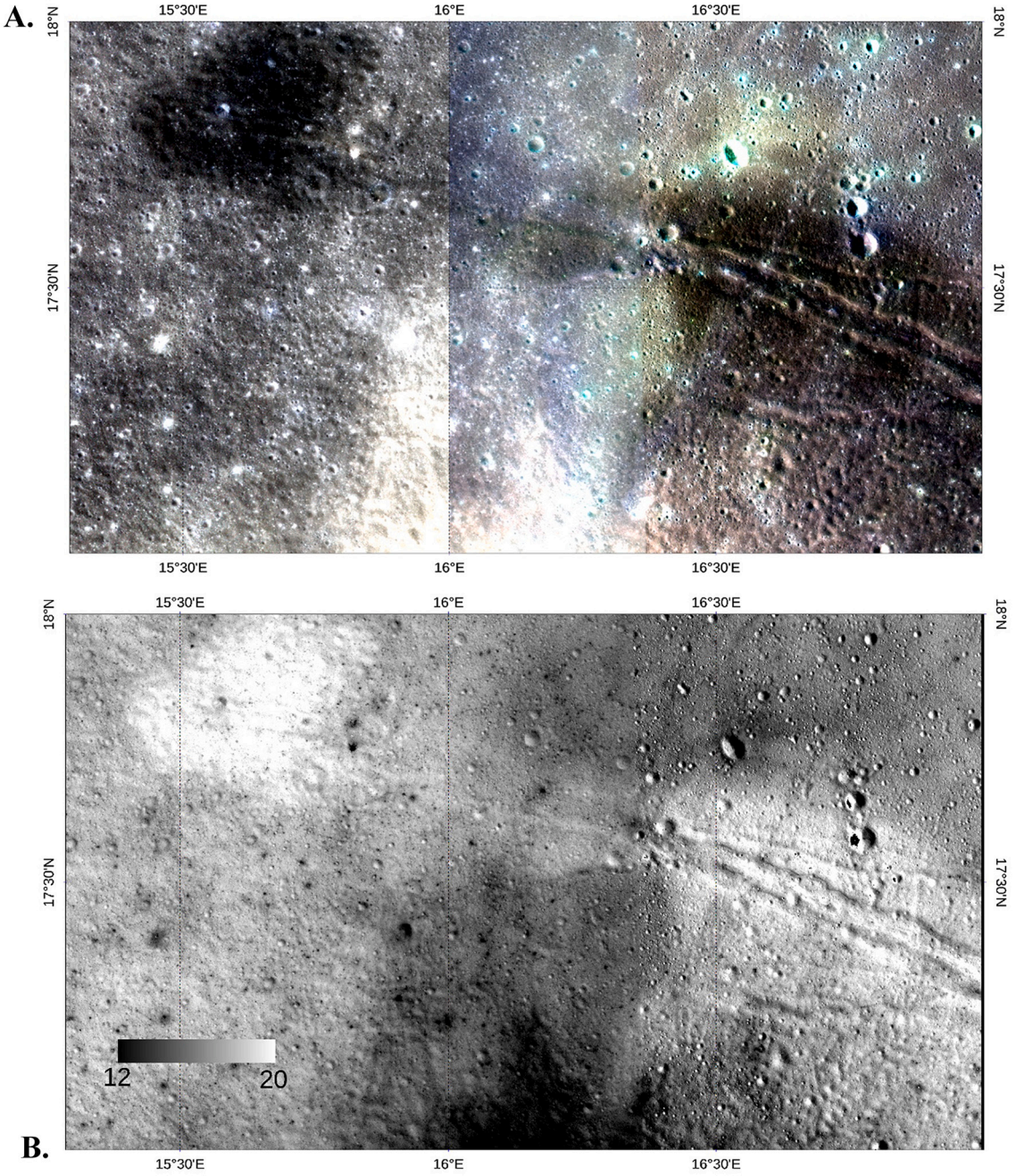

Fig. 5. A. Mosaic of Kaguya MI MAP scenes MI_MAP_02_N18E015N17E016SC and MI_MAP_02_N18E016N17E017SC. Composite of 1001, 950, and 900 nm bands. B. Mosaic of weight percent FeO over Menelaus domes derived via the methodology of Lemelin et al. (2015).

shown in Fig. 3D, indicates that the broader Em map unit is higher in TiO_2 relative to the Mare Serenitatis surface north of it (6 to 8% for the Em unit versus 3 to 5% for the mare to the north). Examination of LROC WAC multispectral data indicates that the Menelaus domes have higher TiO_2 contents than the surrounding Tacquet Formation and the surrounding Em unit. Fig. 4A shows a color composite of the west and east Menelaus domes and the 321 nm/415 nm band ratio for that area is in Fig. 4B. 321 nm/415 nm band ratio is a proxy for TiO_2 content so the higher ratio values in Fig. 4B indicate higher TiO_2 than the surroundings. This is confirmed with reference to the lower spatial resolution (399 m/pixel) TiO_2 map released by the LROC team (Sato et al., 2017) which indicates a maximum value of ~8.9% TiO_2 for the west Menelaus dome (with a mean of 7.2% and a standard deviation of 0.58 over the ROI shown in Supp. Fig. 1) which is comparable to a maximum of 8.5% and mean of 6.4% (and standard deviation of 0.78) for a representative ROI (shown in Supp. Fig. 1) of the broader Em map unit (Fortezzo et al., 2020) and an average of 3.4% TiO_2 (with a standard deviation of 0.83) for a representative ROI (shown in Supp. Fig. 1) of Mare Serenitatis to the north of the TF.

3.2. *Kaguya MI*

Fig. 5A shows a color composite of two mosaiced MI MAP scenes covering the western Menelaus dome and the putative eastern dome. FeO contents derived from Kaguya MI data (Fig. 5B), following the methodology of Lemelin et al. (2015) are in the range of 19 to 20% FeO (vs. 17 to 18% for the immediately surrounding plains). As noted in section 3.1, if the TF does contain a significant pyroclastic component,

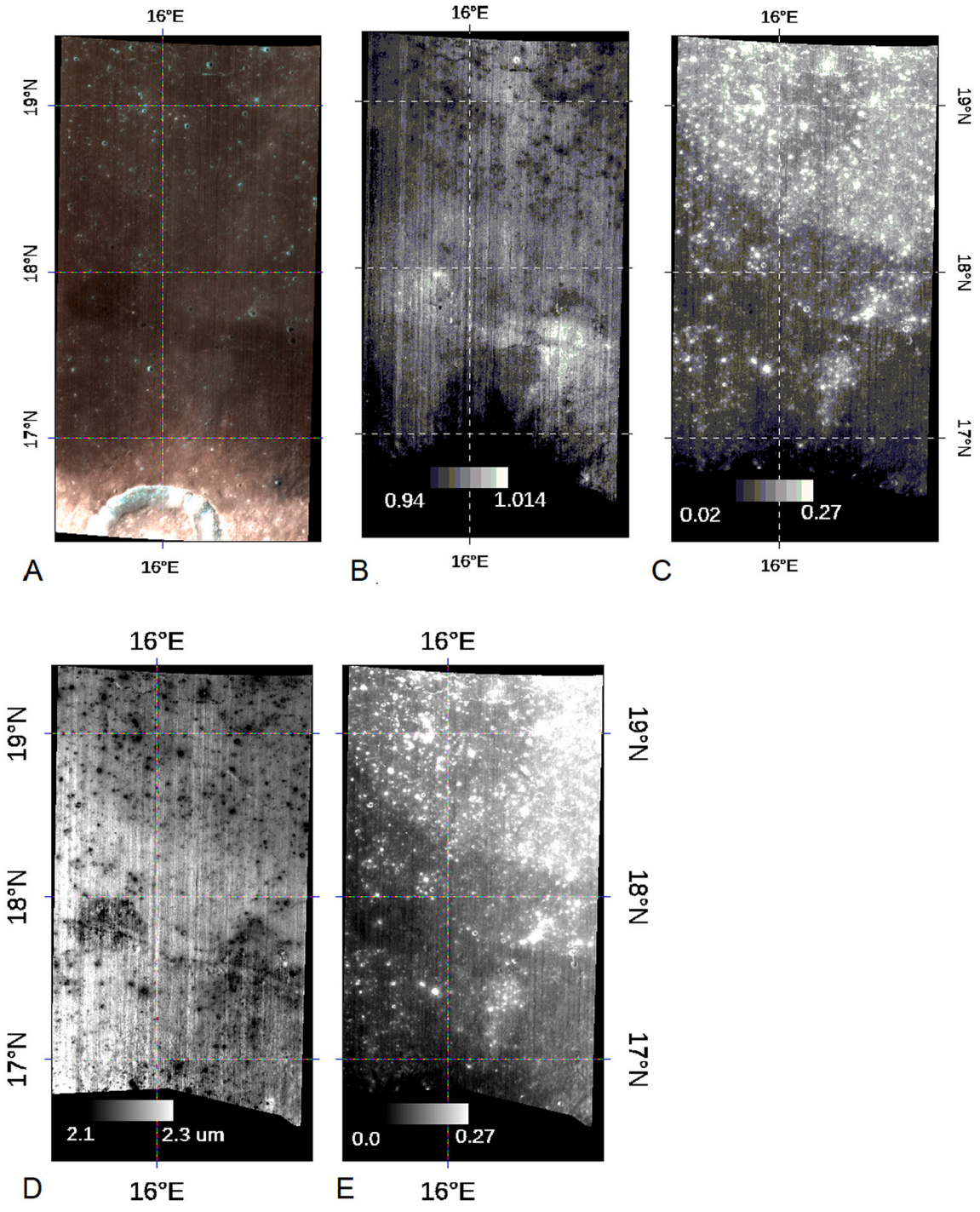

Fig. 6. A. Composite of bands centered at 1.02, 0.75, and 0.58 μm for the M3G20090204T113444 scene that has the TF in lower center and the upper half of Menelaus Crater at bottom center. B. 1 μm band minimum position over the same area as in A (with area over Menelaus crater masked out due to weak to non-existent absorption bands and noise from low value calculations) showing longer 1 μm band center positions over the Menelaus domes and TF. C. 1 μm band depths over the same area. The 1 μm band depths over the TF are commensurate with the surrounding Em map unit. D. 2 μm band minimum position over the same area as in A (showing shorter 2 μm band minimum positions over the Menelaus domes relative to the surrounding Em map unit). E. 2 μm band depths over the same area. The 2 μm band depths over the TF are somewhat shallower than those of the surrounding Em map unit.

the derivation of weight percent FeO from optical data is not quantitative, but the higher values obtained here do indicate a qualitative measure of compositional distinctness of the TF from its surroundings.

3.3. *Chandrayaan-1 M^3*

Since it covers both the west Menelaus dome and the east Menelaus putative dome, an analysis of 1 and 2 μm band parameters was carried out on the M3G20090204T113444 scene. Fig. 6A is an RGB composite showing the domes and the northern rim of Menelaus crater to the south. Using the WM method referenced above, Fig. 6B and D show that the western Menelaus dome has a longer 1 μm band minimum position and a shorter 2 μm band minimum position compared to the surroundings. Over the ROIs shown in Supp. Fig. 2, the mean 1 and 2 μm band center

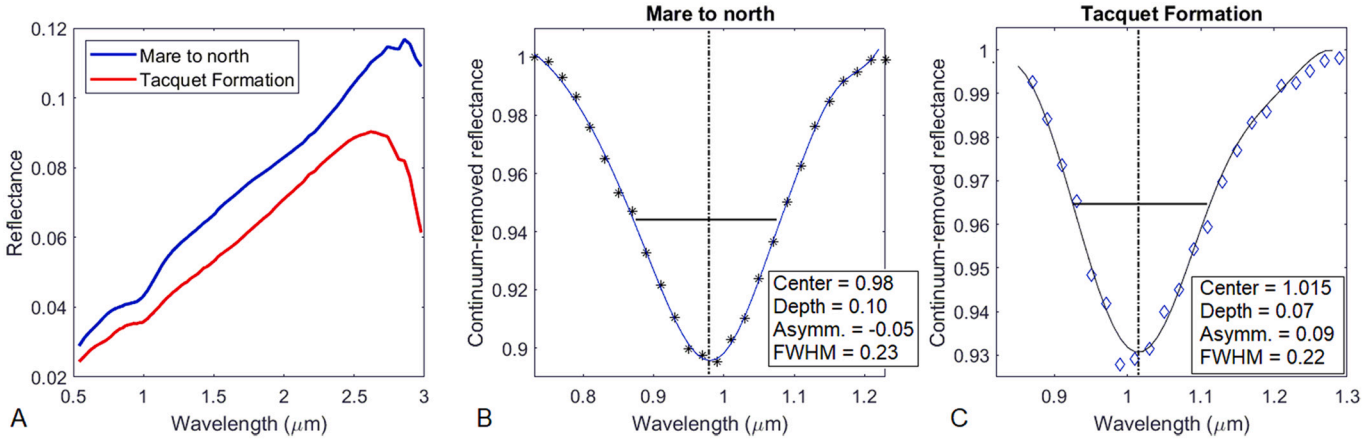

Fig. 7. A. Thermally corrected (via approach of Li and Milliken, 2016) spectra of regions within Tacquet Formation and over the mare to the north. B. Continuum-removed 1 μm region for the mare spectrum with 4th degree gaussian (in blue) fitted to it with band parameters listed in inset. C. Continuum-removed 1 μm region for the Tacquet Formation spectrum with fitted 4th degree gaussian (in black) with band parameters listed in inset. (For interpretation of the references to color in this figure legend, the reader is referred to the web version of this article.)

positions and depths for the west and east Menelaus domes and for the Em map unit and the Mare Serenitatis surface to the north are shown in Supp. Table 1.

In terms of band depth (shown in Fig. 6C and E), the southern Mare Serenitatis basalts have deeper 1 and 2 μm band depths than the Em map unit, and the Menelaus domes/Tacquet formation. Fresh craters, that are not as space weathered, have deeper band depths. The band depth images also highlight the relative lack of craters over the TF (e.g., within the white dash-dot line outlined area in Fig. 3). Crater counts were not performed; however, a relative assessment of the paucity of craters over the TF could be interpreted either as evidence of a younger age and/or as supporting evidence of the presence of a pyroclastic mantling deposit. In examining the pyroclastic mantling deposit west of the Apollo 17 landing site, both Lucchitta and Sanchez (1975) and Gaddis et al. (2011) noted a scarcity of small craters which they attributed to the unconsolidated nature of the pyroclastic deposit.

Fig. 7 shows spectra from regions of interest (ROIs) over the Tacquet Formation and over a portion of the mare to the north. The spectra were thermally corrected via the approach of Li and Milliken (2016) as discussed in the next section. Continuum-removed portions of these spectra over the 1 μm region are shown in Fig. 7B and C. For these spectra, the 1 μm band parameters are also shown. As noted with the WM images in Fig. 6, the TF has a longer wavelength band center position than does the mare and is a weaker band as evidenced by the shallower band depth. However, the full-width at half maximum (FWHM) band width is approximately the same for the two ROI spectra, a fact which will be addressed further in the Discussion section below.

Thermal corrections were carried out on the M3G20090204T094731 scene (which covers the TF to the east of the western Menelaus dome and includes the putative eastern Menelaus dome) with both the approach pioneered by Bandfield et al. (2018) and the Li and Milliken (2016) approach. Then applying the OHIBD band depth mapping to each provides contrasting results. The Li and Milliken (2016) corrected scene (Fig. 8A and B) shows distinctly higher OHIBD values over the TF compared to the surrounding Em map unit (0.036 vs. 0.009; based on ROIs shown in Supp. Fig. 3A). The Bandfield et al. (2018) scene in Fig. 8C and D (using updates described by Tai Udovicic et al., 2021) still shows a modest increase in OHIBD values in the TF relative to the surrounding Em map unit (0.059 vs. 0.039; based on ROIs shown in Supp. Fig. 3B). However, the contrast is much more muted than in the Li and Milliken (2016) corrected data with the starkest contrasts in OHIBD values within Fig. 8D resulting from residual topographic effects in the correction. Higher values of OHIBD occur across the Em map unit and over the Mare Serenitatis surface to the north. Given uncertainties in thermal correction approaches, we examine relative differences between units instead of trying to derive water abundances as has been done in other studies (e.g., Milliken and Li, 2017; Trang et al., 2022). Nevertheless, both OHIBD images in Fig. 8B indicates some level of increase in hydration in the TF relative to the surrounding Em map unit, while the OHIBD in Fig. 8D results in a minor, if any, increase in hydration state above the surrounding terrain. However, neither correction, in their current forms, are likely ideal given the respective treatment of the nature of surface materials, albedo and illumination/viewing geometry. In the Milliken and Li (2017) correction, M^3 data are corrected to laboratory samples that may not accurately represent the spectral character of the deposits in question (e.g., the sampling of lunar pyroclastic glasses returned by the Apollo missions consists of a limited set of samples), while the Bandfield et al. (2018) correction relies on integrated broadband albedo from M^3 data in its derivation of "rough-radiance". The Bandfield et al. (2018) correction requires very well registered topography for its estimation of macro-scale shadowing where even minor pixel-level misregistration could cause the model to either under or over predict "rough-radiances" for areas with modest slopes. Either the effect of topographic misregistration in the Bandfield et al. (2018) correction or a mismatch between available lunar samples and surfaces actually present over the study areas in the Li and Milliken (2016) correction could potentially introduce over or under-estimates of the hydration for either model.

4. Discussion

Several lines of evidence suggest that a pyroclastic mantling deposit covers the Carr (1966) Etd map unit which corresponds to the Tacquet Formation and the Menelaus domes within it. These are summarized in Table 1 and reviewed here. The low circular polarization ratio (CPR) observed by Carter et al. (2009) over the TF is indicative of a fine-grained, mantling deposit and it was stated in that paper that the CPR values were comparable to those of the known Sulpicius Gallus LPD.

Higher FeO has also been cited as a potential characteristic of LPDs. Delano (1986), in his analysis of lunar glasses returned by Apollo astronauts, cited FeO values ranging from 16.5 to 24.7 wt%. Allen et al. (2012) noted FeO values (derived from remote sensing data) for the glass-bearing Aristarchus and Sulpicius Gallus LPDs of 19.3 and 21.6 wt % respectively. Also, Apollo 17 returned samples from the Taurus-Littrow LPD have FeO of 22.7 wt%. The FeO values over the west Menelaus dome from Kaguya MI data (Fig. 5), subject to the uncertainty of the derivation of weight percent FeO over pyroclastic materials noted earlier, are 19 to 20 wt% FeO; thus, this measurement too is consistent

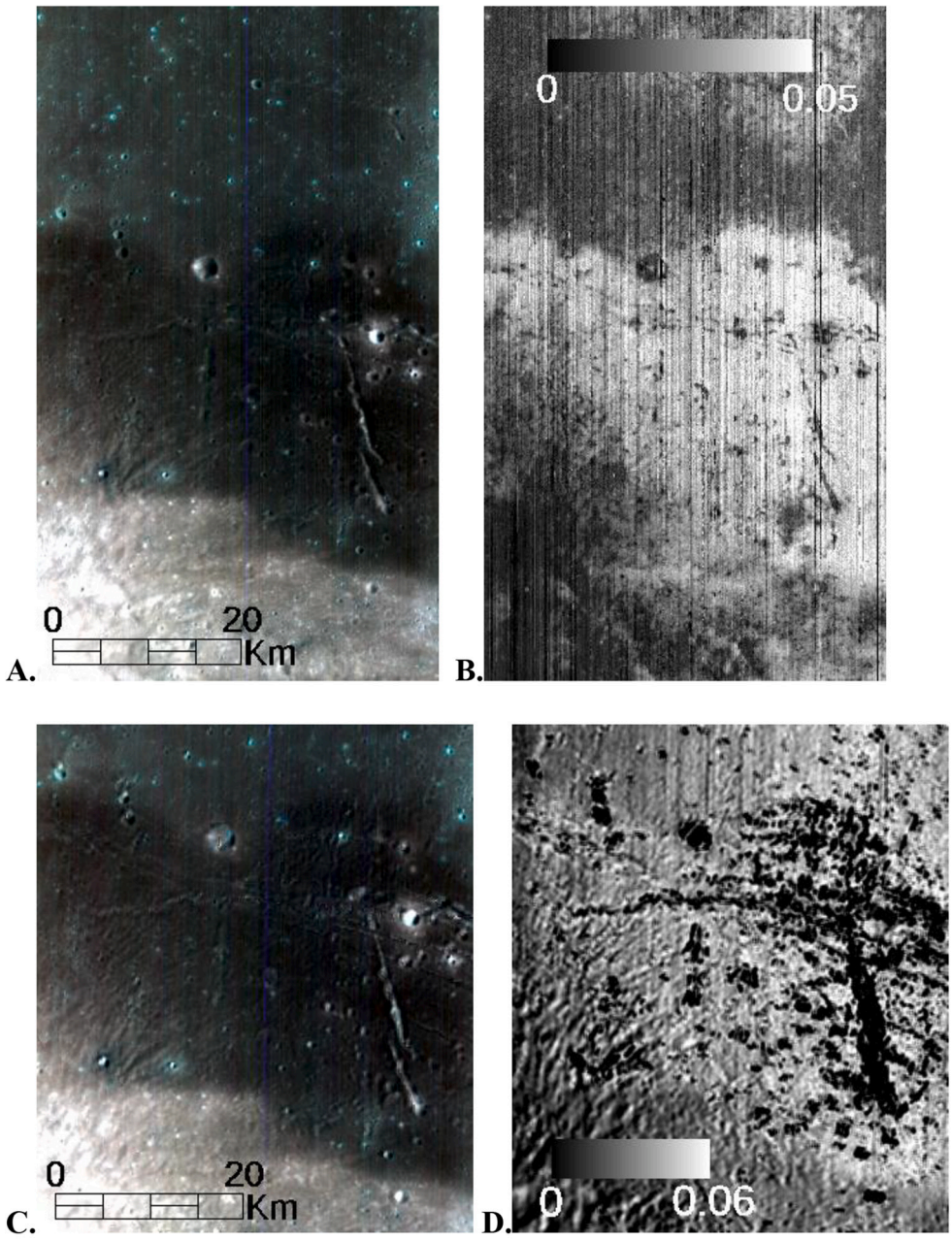

Fig. 8. A. Ungeoreferenced color composite (R = 1.0299, G = 0.7504, B = 0.5808 μm) of subsection of M^3 scene M3G20090204T094731. B. OHIBD image of same subsection using data thermally corrected via the approach of Li and Milliken (2016). C. Approximately the same area but georeferenced using the same color composite band combination. D. OHIBD image using data using the thermal correction approach of Bandfield et al. (2018) as updated by Tai Udovicic et al. (2021). The "high" OHIBD value on the scale bar represents high values within the TF; higher values of OHIBD on sun-facing surfaces are spurious. (For interpretation of the references to color in this figure legend, the reader is referred to the web version of this article.)

with a glass-rich pyroclastic deposit, although not by itself diagnostic of one.

TiO_2 in lunar glasses, as reported on by Delano (1986) is more variable ranging from 0.26 to 16.4 wt%. Given this wide range, the value of ~8.9 wt% TiO_2 derived from LRO WAC multispectral data over the west Menelaus dome cannot be used to support or refute the interpretation of the TF as a pyroclastic deposit. However, the fact that the TF has a 321 nm/415 nm band ratio with values elevated relative to the surrounding Em map unit is suggestive of materials distinct from the latter and presumably a different mode of origin.

Studies have shown that the 1 μm band center of lunar volcanic glasses is shifted to longer wavelengths relative to pyroxenes while the 2 μm band center is shifted to shorter wavelengths (Besse et al., 2014; Moriarty and Pieters, 2016; Runyon et al., 2022; Robertson et al., 2022). Also, a recent study of ilmenite in basaltic mixtures has shown that in ilmenite-bearing basalts there is a similar trend of 1 μm band centers being shifted to longer wavelengths and 2 μm band centers being shifted to shorter wavelengths relative to the band centers of pyroxenes (Robertson et al., 2022). As observed in the Wavelength Mapper images in Fig. 6, such shifts in 1 and 2 μm band center postions are observed for the Menelaus domes and the TF; thus, indicating the possible presence of glass and/or a relatively higher abundance of ilmenite. The possibility of increased ilmenite affecting the band positions could be supported by the higher values of the 321 nm/415 nm ratio over the Menelaus domes shown in Fig. 4. Also, the fact that the TF 1 μm spectrum in Fig. 7C does not have a wider band width does not suggest a pure glass spectrum; however, as shown by Horgan et al. (2014) as much as 85 to 90% of glass is required in a mixture with other ferrous silicate phases for the glass band parameters to clearly be detected. A combination of pyroclastic glass with skeletal ilmenite grains is a potential scenario that could explain the shifts in band center positions.

Finally, while uncertainty remains regarding thermal corrections of the longest wavelengths of the M^3 data, the two approaches examined in this study both indicate increased hydration associated with the TF

Table 1
Features consistent with a pyroclastic mantle as observed over the TF. References refer to observations made over the TF. *Given remaining uncertainties in thermal correction noted in the text.

Feature	Significance	In TF	Reference
Low radar CPR	Unconsolidated mantling deposit	Yes	Carter et al. (2009)
Scarcity of craters (indicated by band depth map)	Unconsolidated mantling deposit	Yes	This study
Higher FeO	Potential association with volcanic glass	Yes	This study
Higher TiO_2	Composition distinct from surroundings	Yes	This study
Longer 1 μm and shorter 2 μm band centers	Potential association with volcanic glass and or increased ilmenite	Yes	This study
Increased OHIBD	Potential association with volcanic glass	Tentatively* yes	This study

relative to surrounding map units. Increased hydration has been attributed to a number of glass-rich LPDs by Milliken and Li (2017); thus, the observation of higher OHIBD values (Fig. 8B) associated with the TF relative to the surrounding Em map unit may be consistent with an origin for the TF as a pyroclastic deposit.

5. Conclusions

The Tacquet Formation (TF) and the Menelaus domes that are contained within it are superimposed on the Eratosthenian mare (Em) unit (Fortezzo et al., 2020) of southern Mare Serenitatis. The TF, as assessed in this paper, is coincident with the Eratosthenian dark (Etd) map unit of Carr (1966) and is found to be unique with regards to the surroundings in terms of several compositional and spectral parameters. These include the TF being higher in FeO relative to the surroundings (as determined from Kaguya MI multispectral data). The TF is also distinct from its surroundings in that it has longer "1 μm" band center and shorter "2 μm" band center positions than the surroundings. Also, by examination of two different thermal correction approaches, the TF has high OH Integrated Band Depth (OHIBD) values- indicative of a deeper OH and/or H_2O band than the surroundings. The TF was examined because Earth-based radar studies (Carter et al., 2009) indicated that it displays low circular polarization ratio (CPR) values consistent with lunar pyroclastic deposits. We find that the compositional and spectral characteristics cited above are also consistent with a glass and/or glass and ilmenite-rich pyroclastic deposit that is younger than the surrounding Em map unit. Thus, Eratosthenian or younger in age. The association of a pyroclastic mantle with the Menelaus domes represents a potentially distinct sub-class of lunar pyroclastic deposits; e.g., one of localized LPDs associated with volcanic domes.

Declaration of Competing Interest

None.

Acknowledgements

This work was conducted under Lunar Data Analysis Program (LDAP) grant 80NSSC20K1428 and with partial funding from LDAP grant NNX16AN63G. Thanks to Dr. S. Li of the University of Hawaii for providing thermally corrected M^3 data over the study area. This manuscript was improved by helpful reviews by Dr. David Trang and an anonymous reviewer and also by a discussion with Dr. David Blewett.

Appendix A. Supplementary data

Supplementary data to this article can be found online at https://doi.org/10.1016/j.icarus.2022.115021.

References

Allen, C.C., Greenhagen, B.T., Donaldson Hanna, K.L., Paige, D.A., 2012. Analysis of lunar pyroclastic deposit FeO abundances by LRO diviner. J. Geophys. Res. 117, E00H28. https://doi.org/10.1029/2011JE003982.

Bakker, W.H., van Ruitenbeek, F.J.A., van der Werff, H.M.A., Zegers, T.E., Oosthoek, J.H. P., Marsh, S.H., van der Meer, F.D., 2014. Processing OMEGA/Mars express hyperspectral imagery from radiance-at-sensor to surface reflectance. Planet. Space Sci. 90, 1–9.

Bandfield, J.L., Hayne, P.O., Williams, J.-P., Greenhagen, B.T., Paige, D.A., 2015. Lunar surface roughness derived from LRO diviner radiometer observations. Icarus 248, 357–372.

Bandfield, J.L., Poston, M.J., Klima, R.L., Edwards, C.S., 2018. Widespread distribution of OH/H_2O on the lunar surface inferred from spectral data. Nat. Geosci. 11, 173–177.

Barker, M.K., Mazarico, E., Neumann, G.A., Zuber, M.T., Haruyama, J., Smith, D.E., 2016. A new lunar digital elevation model from the lunar orbiter laser altimeter and SELENE terrain camera. Icarus 273, 346–355. https://doi.org/10.1016/j.icarus.2015.07.039.

Besse, S., Sunshine, J.M., Gaddis, L.R., 2014. Volcanic glass signatures in spectroscopic survey of newly proposed lunar pyroclastic deposits. J. Geophys. Res. Planets 119, 355–372. https://doi.org/10.1002/2013JE004537.

Carr, M.H., 1966. Geologic map of the Mare Serenitatis region of the moon. U.S. Geol. Surv. Misc. Geol. Invest. Map I-489.

Carter, L.M., Campbell, B.A., Hawke, B.R., Campbell, D.B., Nolan, M.C., 2009. Radar remote sensing of pyroclastic deposits in the southern Mare Serenitatis and Mare Vaporum regions of the moon. J. Geophys. Res. 114, E11004. https://doi.org/10.1029/2009JE003406.

Clark, R.N., Pieters, C.M., Green, R.O., Boardman, J.W., Petro, N.E., 2011. Thermal removal from near-infrared imaging spectroscopy data of the moon. J. Geophys. Res. 116, E00G16. https://doi.org/10.1029/2010JE003751.

Delano, J., 1986. Pristine lunar glasses: Criteria, data, and implications. Proc. Lunar Planet. Sci. Conf. 16th, 201–213.

Fortezzo, C.M., Spudis, P.D., Harrel, S.L., 2020. Release of the digital unified global geologic map of the moon at 1:5,000,000- scale. In: 51st Lunar and Planetary Science Conference, abs. #2760.

Gaddis, L.R., Staid, M.I., Tyburczy, J.A., Hawke, B.R., Petro, N.E., 2003. Compositional analyses of lunar pyroclastic deposits. Icarus 161 (2), 262–280.

Gaddis, L., van der Bogert, C.H., Cheng, Y., Huertes, A., Skinner, J., Hawke, B.R., Giguere, T., 2011. Small crater densities near Apollo 17: clues to properties of lunar pyroclastic deposits. In: 42nd lunar and planet. Sci. Conf. abstract #2584.

Gustafson, J.O., Bell, J.F., Gaddis, L.R., Hawke, B.R., Giguere, T.A., 2012. Characterization of previously unidentified lunar pyroclastic deposits using Lunar Reconnaissance Orbiter Camera data. J. Geophys. Res. 117, E00H25. https://doi.org/10.1029/2011JE003893.

Hapke, B., 2012. *Theory of Reflectance and Emittance Spectroscopy*, 2nd ed. Cambridge University Press, Cambridge. https://doi.org/10.1017/CBO9781139025683.

Hapke, B., Sato, H., Robinson, M., 2019. Lunar reconnaissance orbiter wide angle camera algorithm for TiO_2 abundances on the lunar surface, including the highlands and low-Ti maria. Icarus 321, 141–147.

Hawke, B.R., Coombs, C.R., Gaddis, L.R., Lucey, P.G., Owensby, P.D., 1989. Remote sensing and geologic studies of localized dark mantle deposits on the Moon. Lunar and Planetary Science Conference Proceedings (Vol. 19,, 255–268.

Hecker, C., van Ruitenbeek, F.J.A., Bakker, W.H., Fagbohun, B.J., Riley, D., van der Werff, H.M.A., van der Meer, F.D., 2019. Mapping the wavelength position of mineral features in hyperspectral thermal infrared data. Int. J. Appl. Earth Obs. Geoinf. 79, 133–140.

Horgan, B.H., Cloutis, E.A., Mann, P., Bell III, J.F., 2014. Near-infrared spectra of ferrous mineral mixtures and methods for their identification in planetary surface spectra. Icarus 234, 132–154.

Klima, R.L., Petro, N.E., 2017. Remotely distinguishing and mapping endogenic water on the Moon. Philosoph. Trans. Royal So. A: Mathemat. Phys. Eng. Sci. 375 (2094), p.20150391.

Lawrence, D.J., Feldman, W.C., Elphic, R.C., Little, R.C., Prettyman, T.H., Maurice, S., Lucey, P.G., Binder, A.B., 2002. Iron abundances on the lunar surface as measured by the lunar prospector gamma-ray and neutron spectrometers. J. Geophys. Res. 107, 5130. https://doi.org/10.1029/2001JE001530.

Lemelin, M., Lucey, P.G., Song, E., Taylor, G.J., 2015. Lunar central peak mineralogy and iron content using the Kaguya multiband imager: reassessment of the compositional structure of the lunar crust. J. Geophys. Res. Planets 120, 869–887. https://doi.org/10.1002/2014JE004778.

Lemelin, M., Lucey, P.G., Gaddis, L.R., Hare, T., Ohtake, M., 2016. Global Map Products from the Kaguya Multiband Imager at 512 Ppd: Minerals, FeO and OMAT, 47th LPSC, abs. #2994.

Lemelin, M., Lucey, P.G., Miljkovic, K., Gaddis, L.R., Hare, T., Ohtake, M., 2019. The compositions of the lunar crust and upper mantle: spectral analysis of the inner rings of lunar impact basins. Planet. Space Sci. 165, 230–243.

Lena, R., Wöhler, C., Phillips, J., Chiocchetta, M.T., 2013. Lunar Domes: Properties and Formation Processes. Springer, 174 pp.

Li, S., Milliken, R.E., 2016. An empirical thermal correction model for moon mineralogy mapper data constrained by laboratory spectra and diviner temperatures. J. Geophys. Res. 121, 2081–2107.

Li, S., Milliken, R.E., 2017. Water on the surface of the Moon as seen by the Moon Mineralogy Mapper: Distribution, abundance, and origins. Sci. Adv. 3, e1701471.
Lucchitta, B.K., Sanchez, A.G., 1975. Crater studies in the Apollo 17 region. In: Lunar and Planetary Science Conference Proceedings, 6, pp. 2427–2441.
Lucey, P.G., Blewett, D.T., Jolliff, B.L., 2000. Lunar iron and titanium abundance algorithms based on final processing of Clementine ultraviolet-visible images. J. Geophys. Res. 105, 20297–20305. https://doi.org/10.1029/1999JE001117.
McCord, T.B., Taylor, L.A., Combe, J.-P, Kramer, G., Pieters, C.M., Sunshine, J.M., Clark, R.N., 2011. Sources and physical processes responsible for OH/H_2O in the lunar soil as revealed by the Moon Mineralogy Mapper (M^3). J. Geophys. Res. 116, E00G05 https://doi.org/10.1029/2010JE003711.
McEwen, A.S., Robinson, M.S., 1997. Mapping of the moon by Clementine. Adv. Space Res. 19 (10), 1523–1533.
Milliken, R.E., Li, S., 2017. Remote detection of widespread indigenous water in lunar pyroclastic deposits. Nat. Geosci. 10, 561–565.
Moriarty, D.P., Pieters, C.M., 2016. Complexities in pyroxene compositions derived from absorption band centers: examples from Apollo samples, HED meteorites, synthetic pure pyroxenes, and remote sensing data. Meteorit. Planet. Sci. 51, 207–234.
Ohtake, M., Pieters, C.M., Isaacson, P., Besse, S., Yokota, Y., Matsunaga, T., Boardman, J., Yamamoto, S., Haruyama, J., Staid, M., Mall, U., Green, R.O., 2013. One moon, many measurements 3: spectral reflectance. Icarus 226, 364–374.
Petro, N.E., Isaacson, P.J., Pieters, C.M., Jolliff, B.L., Carter, L.M., Klima, R.L., 2013. Presence of OH/H_2O associated with the lunar Compton-Belkovich complex identified by the moon mineralogy mapper (M^3). 44th Lunar and Planetary Science Conference 2688–2689 abstract #2688.
Pieters, C.M., et al., 2009. The moon mineralogy mapper (M^3) on Chandrayaan-1. Curr. Sci. 500–505.
Robertson, K., Milliken, R., Pieters, C., Tokle, L., Cheek, L., Isaacson, P., 2022. Textural and compositional effects of ilmenite on the spectra of high-titanium lunar basalts. Icarus 375, 114836.
Robinson, M.S., Brylow, S.M., Tschimmel, M., Humm, D., Lawrence, S.J., Thomas, P.C., Denevi, B.W., Bowman-Cisneros, E., Zerr, J., Ravine, M.A., Caplinger, M.A., 2010. Lunar reconnaissance orbiter camera (LROC) instrument overview. Space Sci. Rev. 150 (1–4), 81–124.
Ruitenbeek, Van, et al., 2014. Mapping the wavelength position of deepest absorption features to explore mineral diversity in hyperspectral images. Planet. Space Sci. 101, 108–117.
Runyon, K.D., Nelson, L., Moriarty III, D.P., 2022. Identifying impact melt from the Smythii Basin: toward an improved chronology for Lunar Basin formation. The Planetary Sci. J. 3 (2), 48. https://doi.org/10.3847/psj/ac51e2.
Sato, H., Robinson, M.S., Lawrence, S.J., Denevi, B.W., Hapke, B., Jolliff, B.J., Hiesinger, H., 2017. Lunar mare TiO_2 abundances estimated from UV/Vis reflectance. Icarus 296, 216–238.
Tai Udovicic, C.J., Edwards, C.S., Bandfield, J.L., 2019. Validating a lunar roughness-based thermal correction with Diviner temperature observations. In: AGU Fall Meeting abstract P33F-3500.
Tai Udovicic, C.J., Bandfield, J.L., Ghent, R.R., Farrand, W.H., Edwards, C.S., 2020. Testing lunar near infrared corrections with diviner observations. In: 51st Lunar and Planetary Science Conference abstract #2632.
Tai Udovicic, C.J., Gonzales, J.K., Ruiz, J.A., Edwards, C.S., Haberle, C., Farrand, W.H., Bandfield, J.L., 2021. Predicting emitted radiance of rough lunar surfaces to inform volatile distribution. In: Geological Society of America Annual Meeting, T112, pp. 107–108.
Trang, D., Gillis-Davis, J.J., Lemelin, M., Cahill, J.T., Hawke, B.R., Giguere, T.A., 2017. The compositional and physical properties of localized lunar pyroclastic deposits. Icarus 283, 232–253.
Trang, D., Tonkham, T., Filiberto, J., Li, S., Lemelin, M., Elder, C.M., 2022. Eruption characteristics of lunar localized pyroclastic deposits as evidenced by remotely sensed water, mineralogy, and regolith. Icarus 375, 114837.
Wilcox, B.B., Lucey, P.G., Hawke, B.R., 2006. Radiative transfer modeling of compositions of lunar pyroclastic deposits. J. Geophys. Res. 111, E09001. https://doi.org/10.1029/2006JE002686.
Wöhler, C.A., Grumpe, A.A. Berezhnoy, Shevchenko, V.V., 2017. Time-of-day-dependent global distribution of lunar surficial water/hydroxyl. Sci. Adv. 3, e1701286 https://doi.org/10.1126/sciadv.1701286.